Chapter 3

Structural, Optical and Photocatalytic study of DT500 and DT800

3.1 Importance of diatoms as a photocatalyst

Photo-catalytic degradation has been one of the most promising and economic techniques of the past several decades for the treatment of effluents containing toxic dyes. TiO_2 nano-structure incidentally is a highly suitable material for photocatalytic degradation of dyes. There are very limited published reports on use of light harvesting with naturally available materials to further improve photocatalytic efficiency of TiO_2 nanostructures [1]. Currently, researchers are placing effort on use of hierarchical heterostructures in combination with photocatalysts for increased photocatalytic activity by aiding the separation longevity of photo generated electron-hole (e^--h^+) pairs in these photo-catalysts [2]. Diatoms being natural hierarchical porous silica structures, having spatially ordered and periodic nano to micro size pores; interact with light very efficiently by diffractive processes [3]. These structures can control light propagation by coupling incoming light into distinct waveguide modes passing through their frustules acting as a photonic crystal slab waveguide. Also, these diatom structures can utilize the whole spectrum of optical radiation from ultra-violet to visible light due to the presence of chlorophyll receptors and spectrally sensitive carotenoids [4, 5].

In this work report is being made of a new and novel method of getting higher efficiency photocatalysis by use of TiO_2 nanostructures having anatase and rutile mixed phase templated on diatom frustules, henceforth named DT800. The efficiency is shown to be relatively higher by investigations on the photocatalytic activity of these materials using different dyes, in comparison to single anatase phase TiO_2 nanostructures templated on diatoms, henceforth named DT500 and bare physical mix of TiO_2 powder and diatom frustules, henceforth named $DTiO_2$.The kinetics of heterogeneous photocatalytic reaction for different dyes will also be explained in this chapter.

At first, Methyl orange (MO) was taken as model dye for study of photocatalytic activity of the prepared samples. Methyl Orange (MO) is one such azo dye that is not readily biodegradable. It has various uses in textile industry, printing, colouring certain items, pharmaceutical industries, leather industry, etc. Above a certain quantity it is toxic if swallowed, harmful if inhaled, mutagenic and carcinogenic, can cause eye irritation, skin irritation, irritation of the digestive tract, can increase the heart rate, cause vomiting, damage of lung tissue, etc. [6-9]. Thereafter photocatalytic activity of the as-synthesized catalysts was studied by using Methylene blue (MB) as another model dye.

3.2 Structural characterizations of the photocatalysts

3.2.1 Structural characterization of DT500, DT800 and raw diatom frustules using X-ray diffraction spectra

To analyze the phases present in the prepared samples XRD was employed. The XRD patterns of the samples are shown in Figure 3.1. Also, using A to symbolically represent anatase phase and R to represent rutile phase the diffraction planes were identified from these XRD studies. The peaks at 25.26º, 27.33º,36.08º, 37.70º, 41.16º, 47.94º, 54.16º, 56.47º, 62.58º, 68.80º, 69.60º and 74.89º corresponded to the diffractions at the planes A(101), R(110), R(101), A(004), R(111), A (200), R(211), R(220), R(002), A(116), R(112) and R(320) respectively of the sample DT800 when compared with the standard data obtained from JCPDS no-71.1167 and JCPDS no-89-4920. The peaks 25.37º, 37.90º, 48.07º, 53.94º, 55.20º, 62.80º, 68.91º, 70.42º and 75.20º corresponded to the diffraction at the planes A(101), A(004), A(200), A(105), A(211), A(204), A(116), A(220) and A(215) of the sample DT500 when compared with JCPDS no-71.1167. The absence of rutile peaks in the XRD graph of DT500 confirmed that the titania nanostructures of this catalyst were in anatase phase only. Sample DT800 contained both rutile and anatase phases as was confirmed by the 25.26º and 27.33º peaks. The sharp and intense peaks indicated the high crystalline nature of the prepared samples. The crystallite size (D) was calculated by using the Debye-Scherrer formula given below.

$$D = k\lambda/\beta\cos\theta \tag{3.1}$$

$$\beta = \text{FWHM} \times (\pi/180)^{o} \tag{3.2}$$

where λ is the wavelength of X-ray radiation (Cu Kα, λ= 0.15406Å), k is a constant taken as 0.91, β is the full width at half maximum height (FWHM) of the peak, and θ is the diffraction angle. Plane R(110) of the sample DT800 and plane A(101) of the sample DT500 were chosen to calculate the crystallite size of the samples respectively. The average crystallite sizes were found to be 37.4nm and 14.6nm for DT800 and DT500 respectively. It was also observed that no peaks associated to SiO_2 were found in the XRD plots of diatom samples that were analyzed before templating with titania. This indicated that the major structural material of the diatoms themselves, which is silica (SiO_2), was in amorphous form.

The anatase and rutile percentages were also calculated from the X-ray diffractrogram by using the Spurr equation given in equation 3.3 [10].

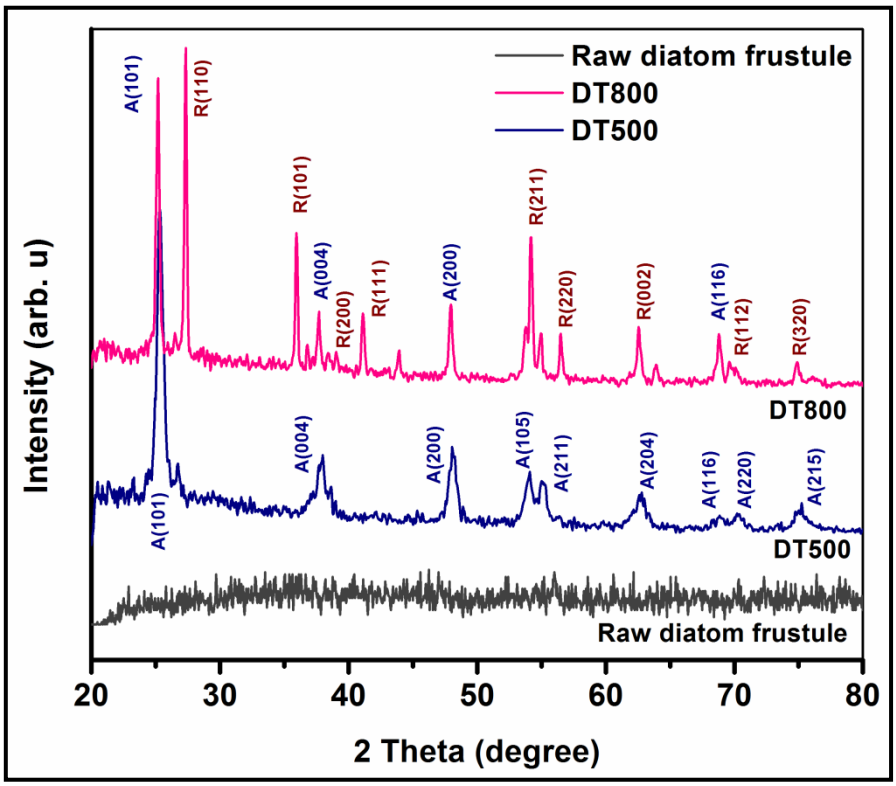

Figure 3.1 XRD patterns of raw diatom frustule, DT800 and DT500 photocatalysts.

$$\%_{Rutile} = 1/\{1 + 0.8(I_A(101)/I_R(110))\} \times 100\% \quad \text{and}$$

$$\%_{Anatase} = 100\% - (\%_{Rutile}) \tag{3.3}$$

where I_A is the intensity of A(101) peak and I_R is the intensity of R(110) peak. The amounts of rutile and anatase phase in the as-synthesized samples are shown in table 3.1.

Table 3.1 Phase composition of the samples calcined at different temperature.

Catalyst name	I_A/I_R	$\%_{Rutile}$	$\%_{Anatase}$
DT500	-	0	100
DT800	0.9155	57.73	42.27

3.2.2 SEM and EDX analysis of DT500, DT800 and raw diatom frustule

The SEM micrographs of diatom frustules were analyzed and compared with the diatom identification guides and ecological data sources. It was confirmed that the diatoms belonged to the *Achnanthidium eutrophilum* species [11]. The cells were about 13μm to 15μm in length and the width was approximately 3μm. Morphology of the diatom frustule templated titania nanostructures are shown in figure 3.2(b and c). Figure 3.2(a) shows a raw diatom frustule. In the valves and girdles of the diatom cell walls, very regular arrays of chambers and pores form periodic patterns. The as-synthesized samples exhibited similar morphology to that of the original diatom frustules (figure 3.2(a)) indicating that the morphology of synthesized diatom templates remain intact. From the SEM micrographs, the average pore size of the frustules was calculated to be approximately 200nm. The Energy Dispersive X-ray spectroscopy (EDX), which was done in conjunction with the SEM analysis, was performed to analyze the % weight, atomic % and characteristic energy levels of the composition of the as prepared samples namely DT500, DT800 and raw diatom frustules and are tabulated in table (3.2, 3.3 & 3.4). EDX spectra in figure 3.3(a, b) showed strong characteristic signal of Ti near 4.5keV for both the samples DT500 and DT800. Peaks observed for Si and O were due to the silica frustules. The weak peak for C was due to the presence of small amount of organic matter.

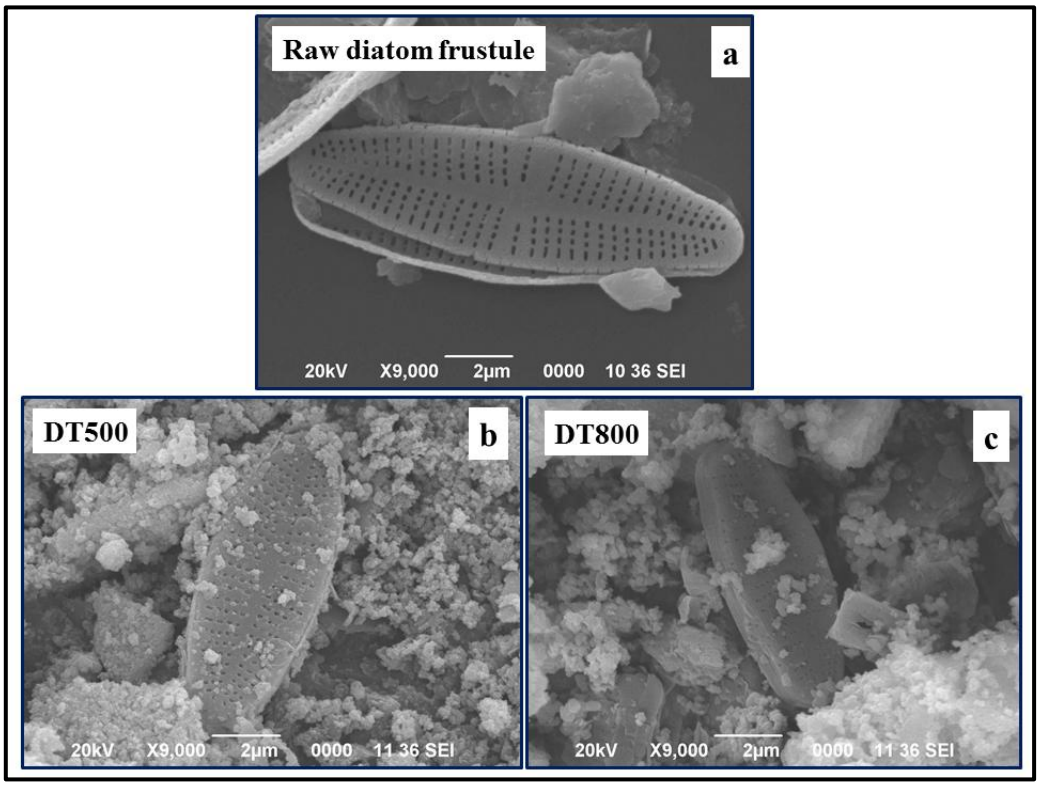

Figure 3.2 SEM images of (a) raw diatom frustule, (b & c) DT500 and DT800 respectively.

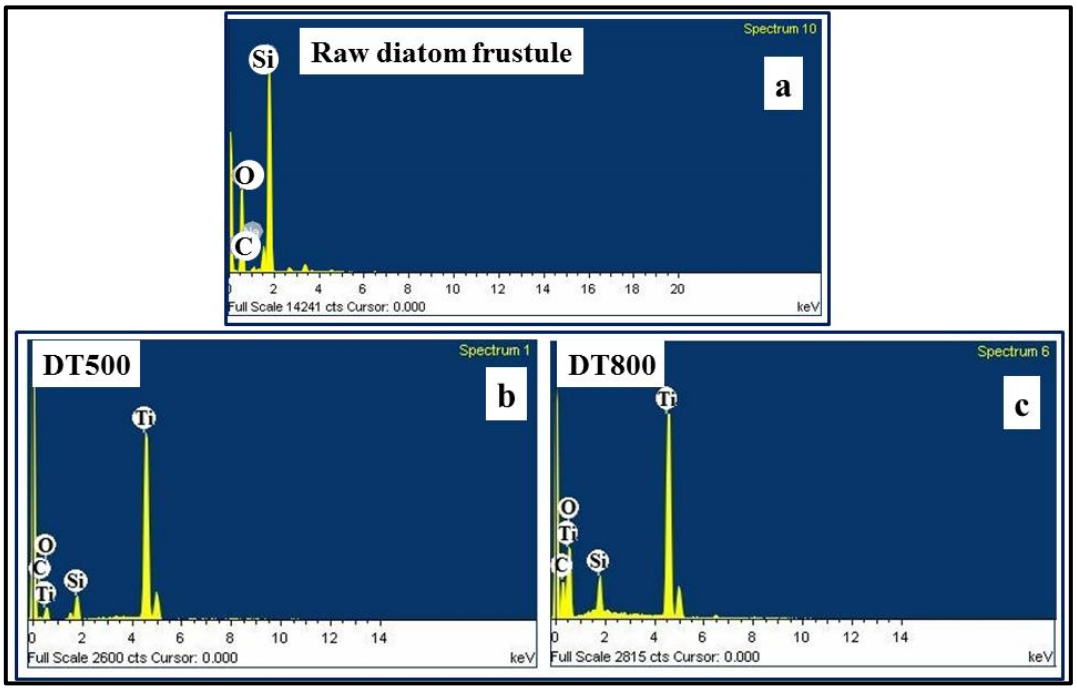

Figure 3.3 EDX spectra of (a) raw diatom frustule, (b) DT500 and (c) DT800 photocatalysts.

Table 3.2 Elemental composition of raw diatom frustule from EDX spectra.

Element	Characteristic Energy levels	Weight (%)	Atomic(%)
C	K	5.16	8.04
O	K	56.79	66.42
Si	K	36.67	24.43
Na	K	1.38	1.12
Total		100.00	

Table 3.3 Elemental composition of DT500 from EDX spectra.

Element	Characteristic Energy levels	Weight (%)	Atomic(%)
C	K	17.11	26.84
O	K	50.65	59.64
Si	K	3.04	2.04
Ti	K	29.20	11.49
Total		100.00	

Table 3.4 Elemental composition of DT800 from EDX spectra.

Element	Characteristic Energy levels	Weight (%)	Atomic(%)
CK	K	13.24	21.44
OK	K	52.39	63.66
SiK	K	3.32	2.30
TiK	K	31.05	12.60
Total		100.00	

3.2.3 TEM analysis of DT500 and DT800

The morphology and size of the as-prepared catalyst were confirmed by TEM analysis which illustrates that, nanoparticles were polycrystalline in nature. From the crystal planes visible in the TEM micrographs shown in figure 3.4(a-d), it could be ascertained that the crystal plane spacing of 0.35nm and 0.32nm corresponded to the inter-planar distance between crystallographic planes of anatase A(101) and rutile R(110) phases of TiO_2 nanostructures respectively (figure 3.4(c, d)). The compositional analysis of DT800 using energy dispersive analysis of X-ray spectroscopy (EDAX), which was done in conjunction with TEM analysis, showed strong characteristic signal of Ti (figure 3.4 (e)). All the peaks except for Cu were attributed to Si, O, C associated with diatom frustules as their fundamental compositional elements.

From TEM micrographs it is observed that the average particle size is small in case of pure anatase nanoparticles and increases with its transformation to mixed phase. For DT500, the particle size distribution is in the range of 9nm to15nm, while for DT800, it is in 20-56nm range as observed from the particle size histogram shown in figure 3.4(f, g) that were obtained using the TEM micrographs. The average particle size is about 14.5nm and 37.5nm for DT500 and DT800 samples respectively, which agrees with the XRD results.

3.2.4 Surface area analysis of DT500 and DT800 by N_2 adsorption/desorption isotherm

The surface texture of DT500 and DT800 samples were also investigated by analyzing Brunauer-Emmett-Teller (BET) N_2 adsorption/desorption isotherm and Berrett-Joyner-Halena (BJH) pore size distribution. In figure 3.5 (c & d) the BJH pore size distributions of DT800 and DT500 catalysts are shown. This distribution plot indicates that both the catalysts have irregular mesoporous pore channels. The surface area and pore diameter of all the samples are given in Table 3.5. The smaller value of effective surface area and pore size of DT800 sample as compared to DT500 sample was due to the blockage of pores by titania nanoparticles deposited in larger amount in DT800 sample than in DT500 sample. Consequently this increased the effective surface area of the trapped A-R titania reactive sites in DT800 catalyst as compared to anatase titania reactive sites in DT500 enhanced the photocatalytic activity in case of DT800 catalyst, which is reported in the succeeding sections. From the N_2 adsorption/desorption isotherms as shown in figure 3.5 (a, b), the catalysts were found to belong to the IUPAC type IV isotherm [12].

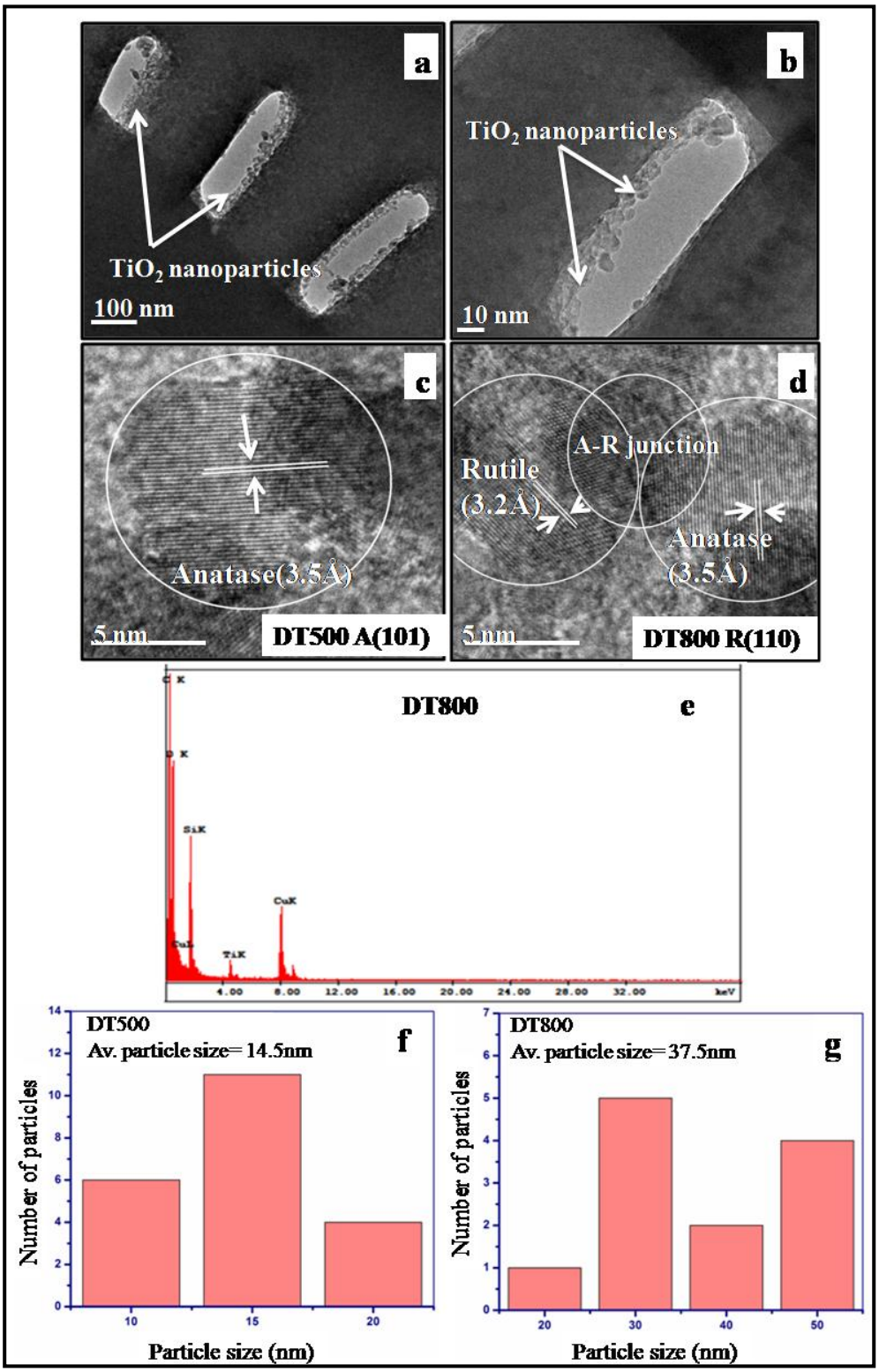

Figure 3.4 TEM images of (a & b) diatom frustule templated titania nanostructures, (c) anatase phase of DT500, (d) anatase-rutile mixed phase of DT800 showing A-R junction, (e) EDAX spectrum of DT800 catalyst, particle size distribution histogram of (f) DT500 and (g) DT800 catalysts.

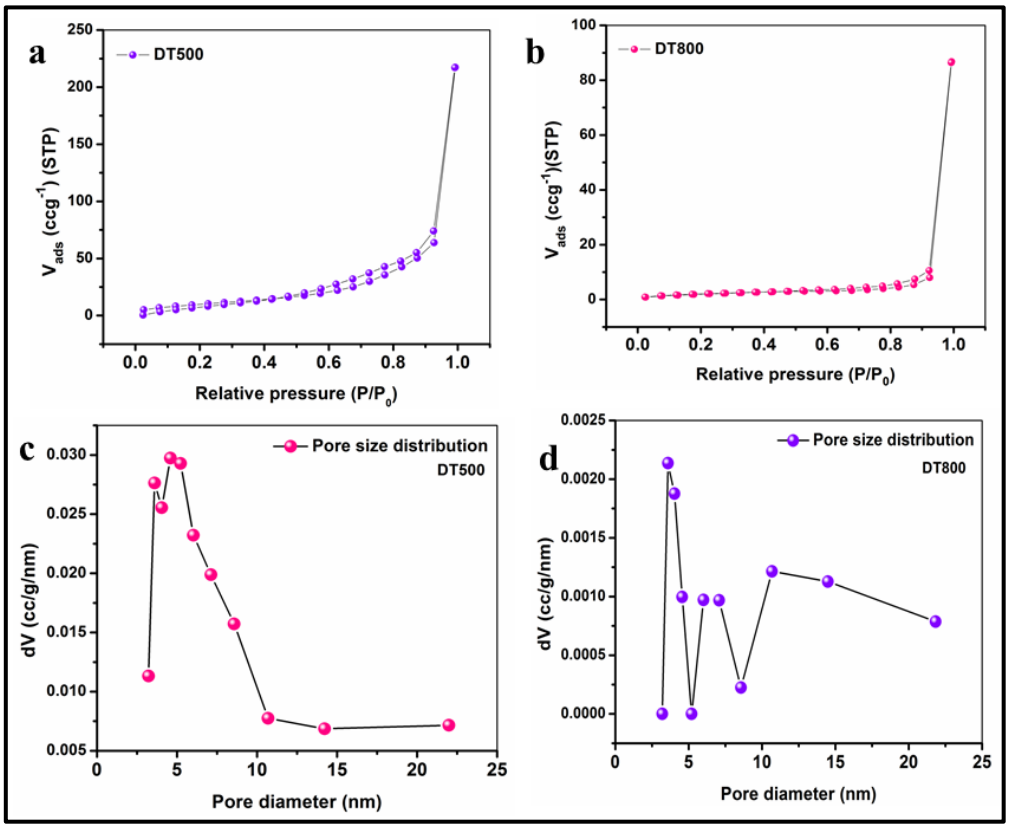

Figure 3.5 (a & b) N_2 adsorption/desorption isotherm and (c & d) BJH pore size distribution of DT500 and DT800 catalysts respectively.

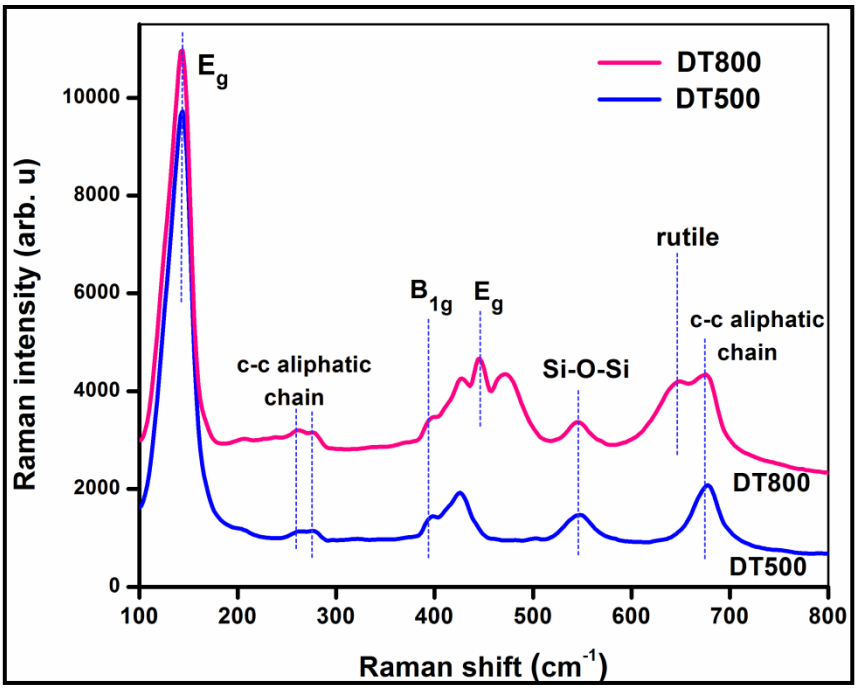

Figure 3.6 Raman spectra of DT800 and DT500 catalysts.

Table 3.5 Surface area and pore size distribution of DT500 and DT800 from N_2 adsorption/desorption analysis

Sample name	Surface area (m^2/g)	Pore diameter (nm)
DT500	64.7	4.59
DT800	7.41	3.59

3.2.5 Raman spectra study of DT500 and DT800

Raman scattering was employed to investigate the evolution of the anatase and anatase-rutile mixed phase in the nano crystals (figure 3.6). The Raman lines at 144cm^{-1} and 396cm^{-1} can be attributed to the E_g and B_{1g} modes of anatase phase respectively for both the samples, where the significantly strong E_g mode at 144 cm^{-1} was due to the symmetric stretching vibration and B_{1g} mode at 396cm^{-1} was due to the symmetric bending vibration of O-Ti-O in the anatase TiO_2 structure [13, 14]. The results indicated the formation of anatase phase of as-synthesized DT500 and DT800 samples and were consistent with the XRD results. When we increased the synthesis temperature upto 800ºC for DT800 sample, the Raman lines for rutile phase modes at 446cm^{-1} and 650cm^{-1} also appeared in conjunction with the anatase phases of TiO_2 nanostructures in the DT800 sample. The peak at 446cm^{-1} corresponded to the E_g mode of the rutile phase [15]. The peak centered at 264cm^{-1}, 278cm^{-1} and 675cm^{-1} were due to C-C aliphatic chain and the peak centered at 546cm^{-1} corresponded to Si-O-Si stretching vibration for both the samples [16]. These aliphatic C-chain and Si-O-Si vibrations occurred due to diatom frustules.

The phonon life time τ can be calculated from energy-time uncertainty relation 3.4 as [17]

$$1/\tau = \Delta E/h = (1/2)\pi c\Gamma \qquad (3.4)$$

where ΔE is the energy uncertainty, Γ is the FWHM of the Raman peaks and h is the Planck's constant. Considering the highest intensity mode E_g for calculating the phonon life time, it was calculated to be 0.84ps for DT500 and 0.89ps for DT800 sample. Presence of contact points between TiO_2 nanostructures of anatase and rutile phases in DT800 increased the formation of grain boundary defect states and hence phonon life time was also increased [18]. Moreover, since size of crystals also has an impact on life time of phonons, the increased crystal size of TiO_2 nanostructures in DT800 enhanced phonon distribution and also increased the phonon life time.

3.2.6 FTIR spectra analysis of DT500 and DT800

In order to determine the different functional groups present in DT500, DT800 and diatom frustules sample; the FTIR spectra were studied in the range of 400-4000cm^{-1} as shown in figure 3.7. Earlier, researchers have observed that the broad band at 400-700cm^{-1} were due to Ti-O-Ti structures[19]. From FTIR spectra, it could be ascertained that the peaks at 531cm^{-1} and 524cm^{-1} were due to Ti-O-Ti stretching vibration for both the samples [20]. Peaks present at 669cm^{-1} and 676cm^{-1} were due to the formation of anatase titania [21]. These peaks were absent in the spectra when FTIR analysis was done with un-templated frustules. For all the samples, peaks present at 1044cm^{-1}, 1043cm^{-1} and 1036cm^{-1} represented asymmetric Si-O-Si vibration in the silica frustules of diatoms [22]. It was ascertained that Ti-O-Si bonds were not formed in the samples as no peak appeared in the range of 910-960cm^{-1}[2]. The peaks at 2864cm^{-1}, 2846cm^{-1} and 2846cm^{-1} were due to alcoxide (CH_2) symmetric stretching mode and those at 2925cm^{-1}, 2926cm^{-1} and 2918cm^{-1} were due to asymmetric stretching mode of the alcoxide [7]. Peaks at 3402cm^{-1}, 3408cm^{-1}, 3394cm^{-1},1637cm^{-1}, 1627cm^{-1} and 1634cm^{-1} were due to the stretching and bending vibration of the -OH group of surface adsorbed water on the samples [21, 23].

Table 3.6 FTIR functional group analysis of DT500, DT800 and raw diatom frustule

Wavenumber (cm^{-1}) of Diatom frustules	Wavenumber (cm^{-1}) of DT500	Wavenumber (cm^{-1}) of DT800	Functional groups	Corresponding structure
---	531	524	Titania	Ti-O-Ti stretching vibration (anatase phase)
1044	1043	1036	Silica	Si-O-Si asymmetric stretching vibration
1637	1627	1634	O-H groups	O-H stretching & bending
2864	2846	2846	C-H groups	CH_2 symmetric stretching
2925	2918	2926	C-H groups	CH_2 asymmetric stretching
3402	3408	3394	O-H groups (Hydroxyl group)	O-H stretching

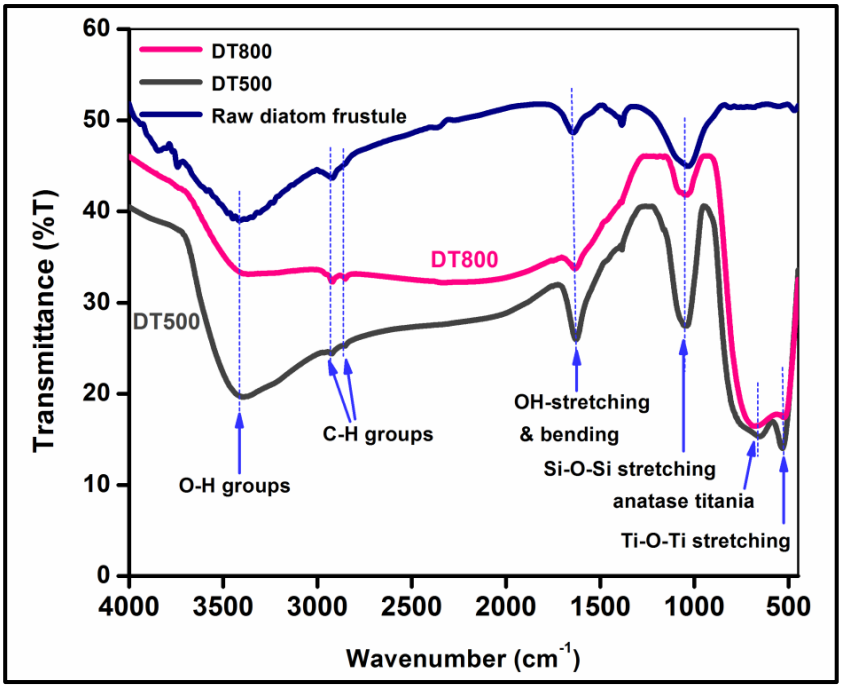

Figure 3.7 FTIR spectra of DT500, DT800 and raw diatom frustules.

3.3 Optical property study of DT500 and DT800

3.3.1 UV-visible absorption spectra analysis of DT500 and DT800

The UV-Visible absorption spectra of DT500, DT800, $DTiO_2$ (a sample formed by physical mixing of diatom frustules and commercially available TiO_2 powder) and diatom frustules calcined at 800°C are shown in figure 3.8. DT500 sample, compared to $DTiO_2$, showed significant increase of light absorption near visible light range due to the band to band transition from 3d levels of Ti to 2p levels of O [18], with increase in intensity and a significant red shift at the absorption edge. DT800 sample showed red shift relative to DT500 with a broad range absorption in the visible light region. Diatom frustules calcined at 800°C showed broad absorption from ultra violet to visible (200nm to about 600nm) range of light. The increase in absorption range in the visible region by the DT500 than $DTiO_2$ samples was due to the diatom frustules that act as template [2] and the even further increase in the absorption range in the visible light region in case of DT800 samples was due to diatom frustules that acted as templates with higher density of defect states (due to mixed anatase-rutile phase) and thereby becoming very efficient in trapping the entire spectrum of visible light. In fact, the red shift in the absorption edge and the increase in the absorption intensity can be attributed to the increased formation rate of e^--h^+ pairs on the surface of the photocatalyst, resulting in improved photocatalytic activity[24].

3.3.2 Evaluation of optical band gap from UV-visible absorption spectra

The optical band gap of all the samples were calculated by using the Tauc relation given below

$$\alpha h\nu = k(h\nu - E_g^{opt})^n \qquad (3.5)$$

where hν is the energy of the incident photon, α is the absorption co-efficient and E_g^{opt} is the optical bandgap energy [25]. The value of n is taken as half (n=1/2), because of direct allowed transitions. Analysis in the band gap using Tauc plot (figure 3.9) indicated that DT500 with pure anatase phase TiO_2 nanostructures and $DTiO_2$ had BGs of 3.2 eV and 3.3 eV in the UV region respectively; whereas DT800, having a mixture of anatase-rutile phase TiO_2 nanostructures, had lower band gap of 3.0eV (Table 3.7) and the BG corresponded to the visible region. The anatase-rutile contact points in DT800 possess defect states in their energy bands which perturbs the band structure. Defect states occur as tail in the band edge referred to as Urbach tail and the energy associated with it is called Urbach energy. The increase in particle size in case of DT800, as observed from TEM images, was also a possible cause for decrease of the BG energy.

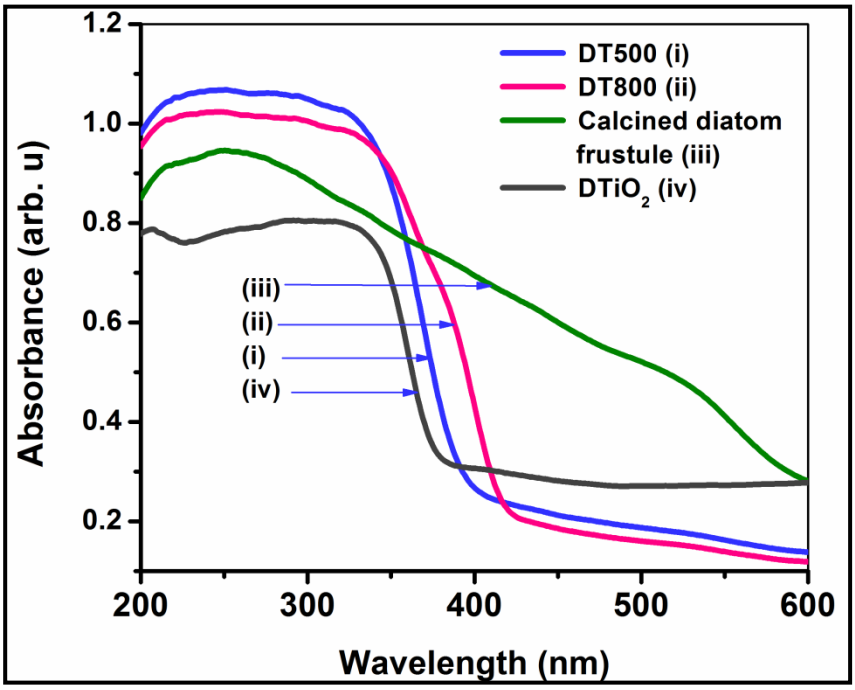

Figure 3.8 UV-vis absorption spectra of DT500, DT800, $DTiO_2$ and diatom frustules calcined at 800°C.

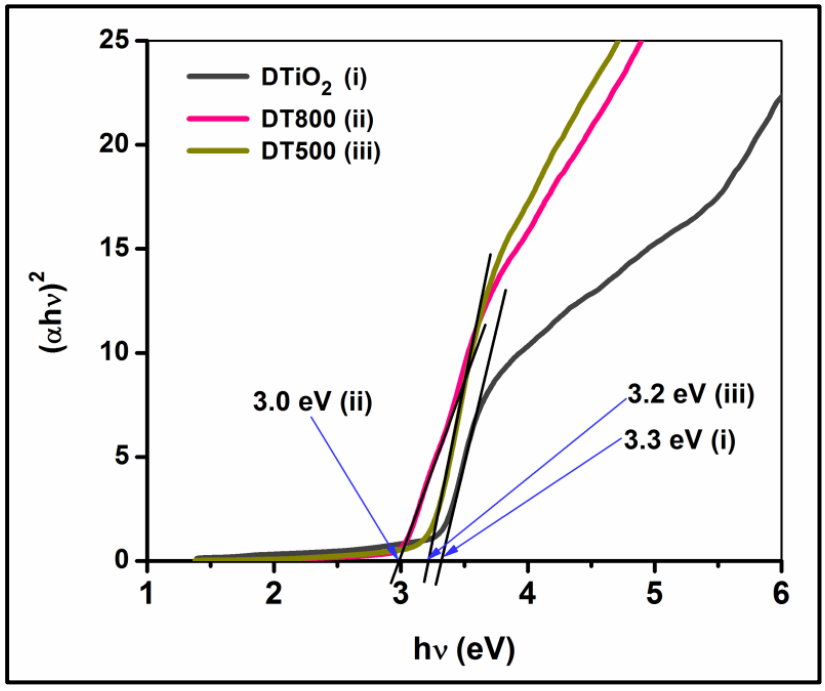

Figure 3.9 Tauc plot showing the band gap of $DTiO_2$, DT800 and DT500 catalysts.

3.3.3 Evaluation of Urbach energy from UV-visible absorption spectra

To measure the structural disorder present in the as-synthesized materials, the Urbach energy was calculated by the following formulae.

$$\alpha = \alpha_o \exp(E/E_U) \tag{3.6}$$

$$\ln(\alpha) = \ln(\alpha_o) + E/E_U \tag{3.7}$$

where α, E and E_U are the absorption co-efficient, photon energy and Urbach energy respectively. Here E is in units of eV. The plot of ln (α) vs E was used to calculate the Urbach energy value (figure 3.10). The reciprocal of the slope of the linear portion in the plot below the optical gap gives the Urbach energy. The calculated E_U values for DT500 and DT800 samples were 325.8meV and 342.7meV respectively as given in table 3.7. The increase in Urbach energy was attributed to the increase of density of oxygen atom vacancies within the TiO_2 nano particles due to breaking of Ti-O bonds. In case of TiO_2 nanoparticles, Ti^{4+} is surrounded by six oxygen ions forming the TiO_6^{2-}octahedra [26]. When it was calcined at high temperature (800°C), Ti-O bond broke and generated considerable amount of oxygen defects by altering the arrangement of oxygen ions around Ti^{4+} and hence increased the oxygen vacancy.

Table 3.7 Optical band gap values and corresponding Urbach energy values of DT500 and DT800

Catalyst name	Calcined Temp(ºC)	Band gap (eV)	Urbach Energy(meV)
DT800	800	3.0	342.7
DT500	500	3.2	325.8

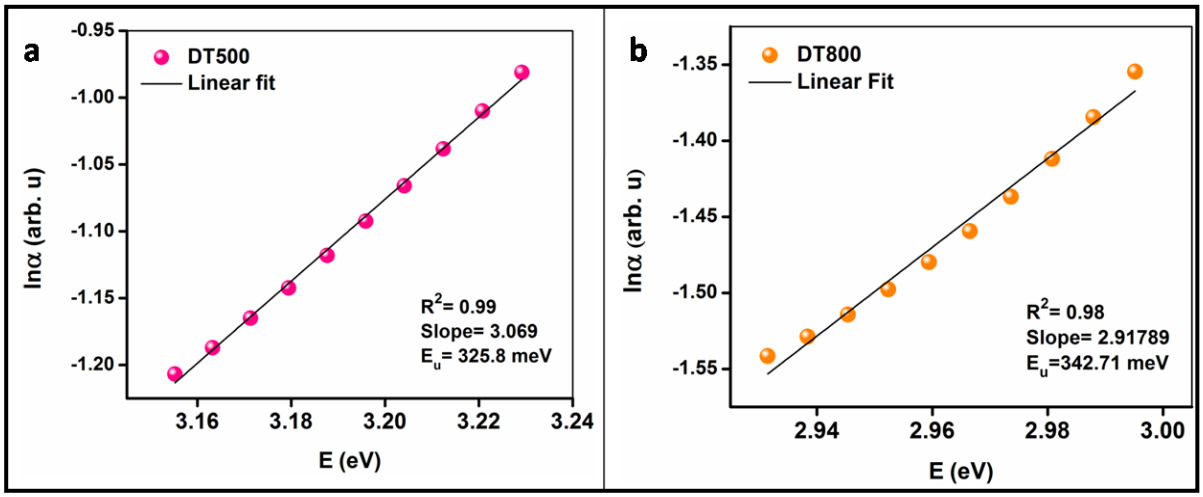

Figure 3.10 Urbach energy determination plots for (a) DT500 and (b) DT800 catalysts.

3.4 Photocatalytic activity study

3.4.1 Evaluation of photocatalytic activity using Methyl Orange as a model dye

As mentioned in section 2.5 in chapter 2, the photo catalytic activity of the as-synthesized materials was studied by observing the changes of absorption spectra in UV-Vis range of MO. The absorption spectra of 10μM solution of MO in presence of DT500, DT800 and $DTiO_2$ are shown in figure 3.11(a, b & c). The spectrum ranged from 350nm to 550nm having maximum absorption at wavelength 464nm. The characteristic absorption peak intensity of MO decreased with the increase of irradiation time. The degradation efficiency of the catalysts was calculated using the following formula [27].

$$\%D = \{(A_0 - A_t)/A_0\} \times 100\% \quad (3.8)$$

where A_0 is the initial absorbance and A_t is the absorbance at time t. The %D vs time plots are shown in figure 3.11(d).

On comparison, it was observed that after 3 hours of irradiation the degradation of MO was approximately 99.12% when catalyst DT500 was used; whereas, degradation of MO achieved by using catalyst DT800 was 99.18% in just only 2 hours of irradiation. Any increase in irradiation time after 3 hours in case of the DT500 samples and 2 hours in case of the DT800 samples was not significant as the absorption spectra in both the cases after these periods were almost flat and negligible. Also the degradation of MO using catalyst $DTiO_2$ was observed to be approximately 82% after 5 hours of light exposure which is significantly lesser than that observed in case of catalysts DT500 and DT800.The change of color from orange to colorless MO solution in presence of the catalysts is presented in figure 3.11 (e & f). The absorption spectra of MO in presence of diatom frustules calcined at 800ºC under same conditions was also observed. No degradation of MO in the presence of diatom frustules was observed. Also, no self-degradation of the dye in isolation, when exposed to light, was observed in our study.The baseline shifts in the plots in figure 3.11(b & c) takes place due to initial increase in turbidity probably due to trace amount of residual catalyst getting left behind in the aliquot even after centrifuge and careful filtration, when a part of the sample was collected for UV-Vis spectral analysis for measuring its degradation.

Titania (TiO_2) nanostructures templated by siliceous porous frustules of diatoms exhibit visible-light activity by shifting the absorption edge from UV range to the visible

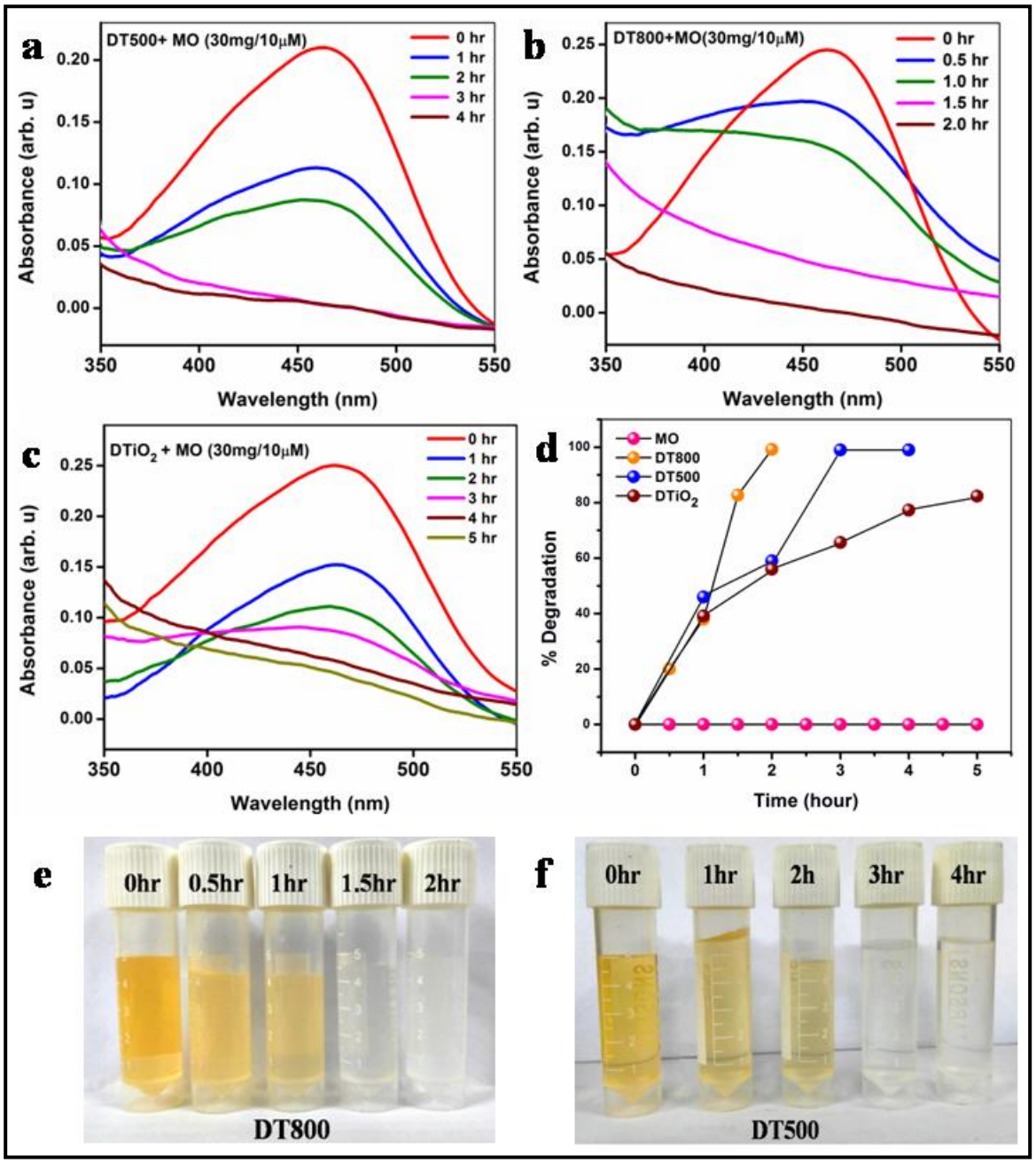

Figure 3.11 Absorption spectra of 10μM solution of MO degraded by (a) DT500, (b) DT800 and (c) $DTiO_2$, (d) Percentage degradation measurement plots of MO using DT500, DT800 and $DTiO_2$ as catalysts, decoloration of MO at different photodegradation times for (e) DT800 and (f) DT500 under light exposure.

light range by showing definite absorption in the visible region (figure 3.8). Also from the Tauc plot in figure 3.9 it was found that BG energy of diatom frustules templated with TiO_2 nanostructures decreases from 3.2eV to 3.0eV which corresponds to visible light in the blue range. The unique morphology of diatom's hierarchical structure along with the phases of DT500 and DT800 are important factors for enhancement of photocatalytic activities. Main factors on which the photocatalytic activity depends are (i) crystalline phase, (ii) surface area and (iii) hierarchical structure [28]. Diatom frustules possesses regular array of chambers (areolae) and pores (cribra). The hollow chambers of these diatom frustules can trap dye molecules because of pores present in the walls of diatoms which allow the dye molecules to pass easily and get trapped inside these hollow chambers. The dye molecules inside the chambers have more opportunity to come in contact with templated titania nanostructures. Also the multiple reflection of light occurring inside the chambers enhanced the photocatalytic activity that resulted in efficient degradation of the dye [2]. Diatoms have the ability of focusing and channeling light. Periodic nanopores present on the surface of diatom frustules can scatter light and subsequent superposition of such periodically scattered light gives rise to focusing effect [29] that help silica hierarchical structures to transmit and channelize more light into the light sensitive titania nanostructures for increased photocatalytic activity. The inter connected porous framework of these hollow structured diatom frustules gives rise to a suction effect, experienced by the dye molecules, which may be attributed to increased adhesive attractive force between the abundant surfaces inside these hollow structures and the dye molecules. This increases the diffusion of dye molecules straight to the reactive sites and traps them alongside the catalytic TiO_2 nanostructures. Therefore, with more titania nanostructures deposited within the porous region of these frustules as observed from BET analysis (figure 3.5), an increased amount of reactive sites was expected and thereby an increase of photocatalytic activity was also expected.

Composites having two phases of same compound is always more effective for enhancement of photocatalytic activity because of reduced recombination rate [28] of photo-generated carriers. Our reported sample DT500 contained only anatase phase and DT800 contained both anatase and rutile phase. In the photocatalytic process, after light absorption by host TiO_2 nanostructures, electrons and holes were formed which combined with water molecules, -OH radicals and water dissolved oxygen molecules to form the hydroxyl radicals and

super oxide anions. These hydroxyl radicals and super oxide anion act as the potential agents in the photodegradation process.

Heterogeneous photocatalysis starts with the photo generation of e^- - h^+ pairs. The mechanism of heterogeneous photocatalysis is shown below [6, 18].

Step 1: Photon (hν) absorption by catalyst:

$$h\nu + \text{catalyst} \rightarrow \text{catalyst}\ (h^+ + e^-) \qquad (h\nu \geq E_g)$$

Step 2: Oxidation of water by photo-generated holes and generation of hyper-reactive hydroxyl free radical:

$$h^+ + H_2O \rightarrow H^+ + \bullet OH\ (\text{hyper} - \text{reactive hydroxyl free radical})$$

$$2h^+ + 2H_2O \rightarrow 2H^+ + H_2O_2$$

$$H_2O_2 \rightarrow 2 \bullet OH$$

Step 3: Reduction of oxygen by photo-generated electrons and generation of hyper- reactive hydroxyl free radical:

$$e^- + O_2 \rightarrow \bullet O_2^-$$

$$\bullet O_2^- + 2H_2O + H^+ \rightarrow H_2O_2 + O_2$$

$$H_2O_2 \rightarrow 2 \bullet OH$$

Step 4: Degradation of reactant species (R) by hyper-reactive hydroxyl free radicals, super oxide anions and photo-generated holes:

$$R + \bullet OH \rightarrow R'^{\bullet}\ (\text{degraded product}) + H_2O$$

$$R + \bullet O_2^- \rightarrow R^{-\bullet}\ (\text{degraded product})$$

$$R + h^+ \rightarrow R^{+\bullet}\ (\text{degraded product})$$

The generated hydroxyl free radicals and super oxide anions interact with the MO molecules and thereby degrade the dye molecules. From the photocatalytic percentage degradation curve (figure 3.11(d)), DT800 was found to exhibit better degradation compared to DT500 and DTiO_2. During photon absorption e^- - h^+ pairs were generated at both anatase and rutile phase of titania. At the junction of anatase and rutile phases of titania embedded on diatom frustules, as shown in the TEM image (figure 3.4(d)), due to slight BG differences between these two phases the conduction band (CB) and valance band (VB) of rutile phase are slightly at higher energy than that in anatase phase. So, the photogenerated e^-s were transferred from the CB of

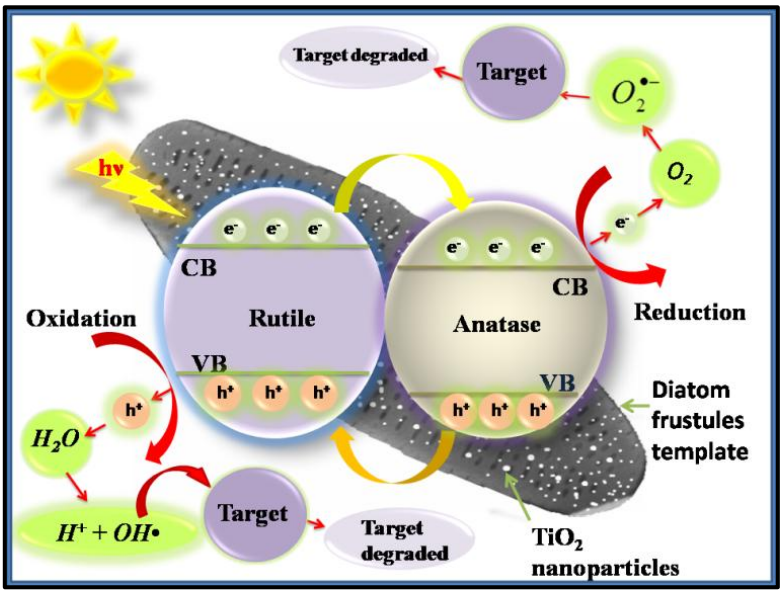

Figure 3.12 Schematic diagram showing oxidation and reduction reactions in photocatalyst having mixed phase.

rutile to the CB of anatase phase. Similarly, the photogenerated h^+s were transferred into the VB of rutile from the VB of anatase phase. This charge transfer phenomenon increased the e^- density in CB of anatase phase and h^+ density in VB of rutile phase decreasing the recombination rate of e^- - h^+ pairs. Thus, in mixed phase titania nanostructure embedded on diatom frustules, charge separation became more stable leading to confinement of the electrons and holes separately and hence readily form hyper reactive radicals which helped in photodegradation phenomenon[30]. The schematic diagram (figure 3.12) shows the entire electron-hole transfer mechanism during the photocatalytic process in the mix phase photocatalyst.

3.4.2 Analysis of reaction kinetics

The kinetics of heterogeneous photocatalytic reaction can be explained by different mechanisms. However, for heterogeneous catalysis Langmuir-Hinshelwood (L-H) mechanism is preferred as can be seen in many reports [31- 33]. In this work, L-H mechanism, first order kinetics and polynomial regression have been studied to explain the kinetics of the photocatalytic reactions involved [32-34]. In L-H mechanism the reaction rate is given by

$$\text{Rate} = -\frac{dC}{dt} = K_R \frac{K_{ad} C}{1 + K_{ad} C} \tag{3.9}$$

where K_R is the rate constant and K_{ad} is the adsorption co-efficient, C is the concentration of dye solution. If the solution is highly diluted, i.e. C (mol/l) < 10^{-3}, like in our case, then $K_{ad}C << 1$ and we can rewrite equation (3.9) as

$$-\frac{dC}{dt} = K_R K_{ad} C = K_r C \tag{3.10}$$

where K_r is the apparent rate constant (RC) of a pseudo first order reaction. Applying boundary condition $C=C_0$ at t=0, and integrating equation (3.10) we get

$$\ln\left(\frac{C_0}{C_t}\right) = K_r t \tag{3.11}$$

As the reactant concentration, in this study, was very low we could use equation 3.11 to determine the value of K_r. Also using the relation between absorbance and concentration of the solution (Beer-Lambert law) a similar expression 3.12 could be used to obtain the value of RC through logarithmic regression using the experimental data [33, 34].

$$\ln\left(\frac{A_0}{A_t}\right) = K_r t \tag{3.12}$$

In figure 3.13 plots of $\ln\left(A_0/A_t\right)$ vs t for the photocatalytic degradation using catalysts DT500 and DT800 are given. Both linear and polynomial regression of the plots in figure 3.13 were studied. From the linear fitting the RC values were determined. The RC values are tabulated in table 3.8 along with the polynomial equations and R^2 values. It was observed that polynomial fitting was better than linear fitting which suggest that L-H mechanism was not suitable to explain the kinetics of the reactions. The larger value of coefficient of the square term (x^2) indicated better degradation of the dye [34]. The acceleration effect of the reaction was probably due to the fact that as the reaction proceeds the concentration of the dye became less and relatively more active sites and surface area became available for catalysis. Hence relatively more number of exciton pairs were available for the remaining dye molecules which then degrade faster than before. The RC represents a measure of how fast or slow the reaction progresses. Larger the value of RC, faster is the reaction.

Table 3.8 Determination of RC for photocatalytic reaction using dye MO

Catalyst name	**Correlation function R^2**		**Polynomial equation**	**RC (hr^{-1})**
	Linear fitting	**Polynomial fitting**		
DT500	0.94	0.95	$y= 0.1440x^2 + 0.4996x$	1.15
DT800	0.92	0.99	$y= 1.19384x^2 – 0.49086x$	2.03

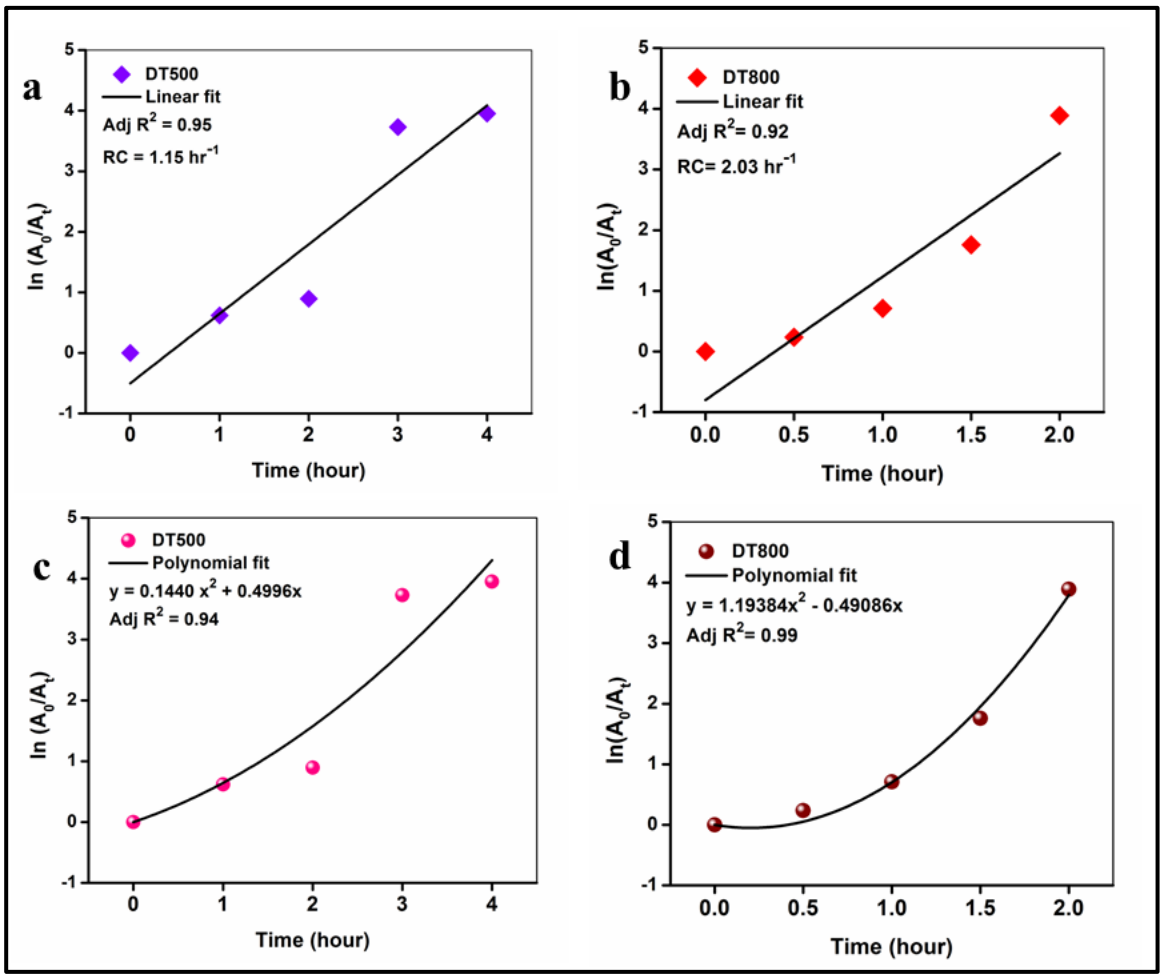

Figure 3.13 Plot to study the kinetics of the catalytic reactions of MO degradation by (a & c) DT500 and (b & d) DT800 by using linear and polynomial regression.

3.4.3 Reusability and durability study of DT800

In order to investigate the reusability and durability properties, DT800 sample only was considered because this catalyst showed significant enhanced property as photocatalyst. The catalysis experiments were performed 5 times using the same DT800 sample under the same conditions as described in this work. After each cycle the sample was separated and cleaned for next experiment. Finally, after 5 cycles of catalytic reactions the sample was cleaned with distilled water and dried properly for further investigation of its properties. The collected catalyst, renamed as DT800*, was characterized by using UV-Vis spectrometer, EDX and TEM to investigate if any changes occurred in its properties. However, it was observed from the EDX spectrum (figure 3.14(b)) that the composition of the material did not change significantly showing characteristic peaks for Ti, Si and O signifying the presence of these elements in the sample. By analyzing the UV-Vis spectrum (figure 3.14(c)) it was observed that the nature of absorption of light by DT800* remained unchanged from that of DT800. Also TEM image (figure 3.14(a)) confirmed the presence of TiO_2 nanoparticles that remained intact with the pores of diatom frustules. These outcomes revealed that the sample properties did not change significantly during many cycles of photocatalysis experiments which confirmed that the catalyst could be reused. The main reason behind this was that the titania nanoparticles that got trapped inside the pores of the frustules exhibited strong attachment and immobilized the nanoparticles, and hence gave rise to mechanical stability. Also, since the catalyst did not dissolve in water, it could be easily separated out from the solution after photocatalytic process.

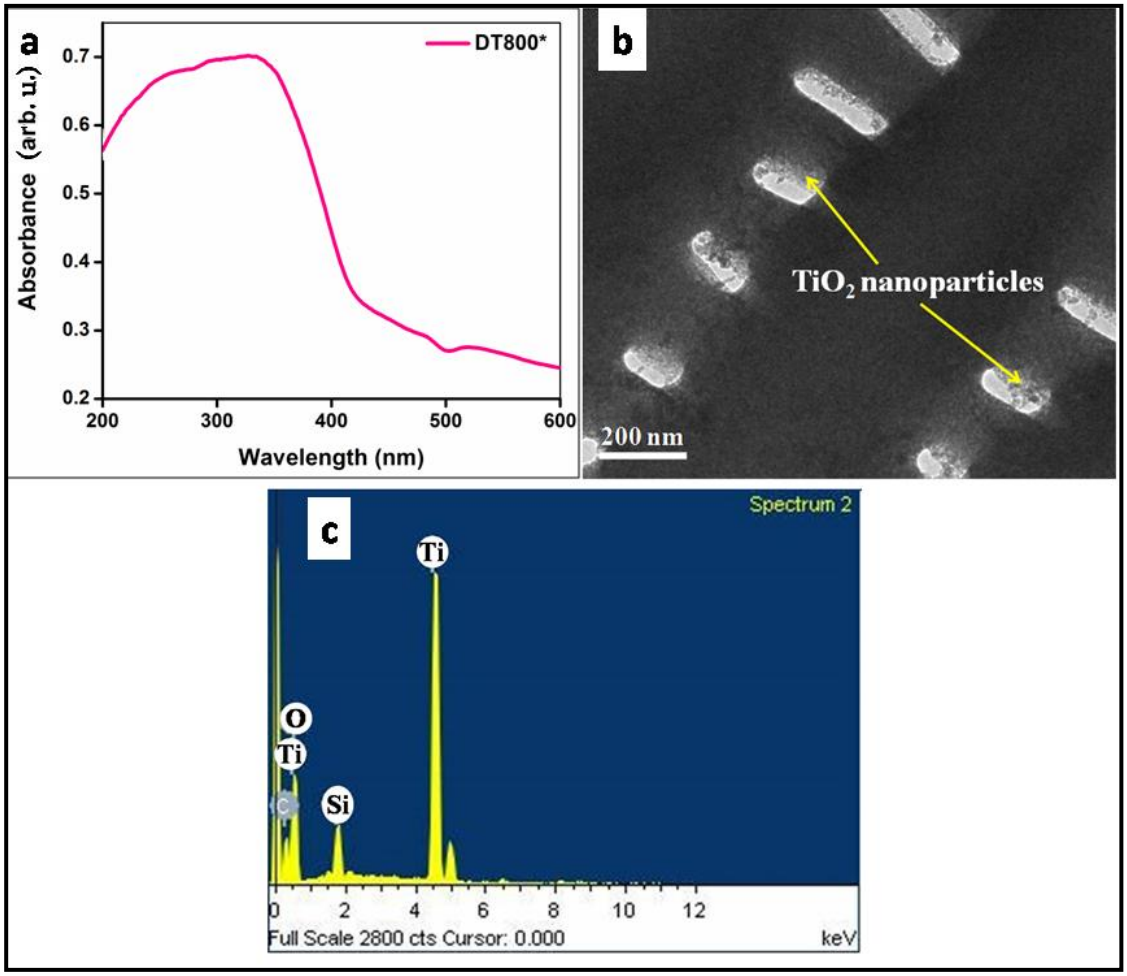

Figure 3.14 (a) UV-vis absorption spectrum, (b) TEM image showing titania nanoparticles inside the pores of diatom frustules and (c) EDX of DT800*.

3.4.4 Evaluation of photocatalytic activity using Methylene Blue as a model dye

The photo catalytic activity of the as-synthesized materials was also studied by observing the degradation of absorption peaks under visible light irradiation in the UV-Vis spectra of MB. The absorption spectra of MB in presence of DT500 and DT800 with 20μM and 50μM dye concentration under visible light irradiation are shown in figure 3.15. The spectrum ranges from 400nm to 800nm with maximum absorption at wavelength 664nm. The characteristic absorption peak intensity of MB decreased with the increase of irradiation time via photocatalysis. Catalyst DT500 degraded MB upto 98% in 40 minutes of irradiation while catalyst DT800 degraded MB upto 98% in just 30min of irradiation for 20μM dye concentration. With increase in dye concentration more time was needed by the same amount of catalyst to degrade the dye. In this case also DT800 was found to be more efficient. For 50μM MB solution, using catalyst DT500, 98.75% degradation occurred in 90 minutes and using DT800 it took 60 minutes for 99.68% degradation, after which the absorption peak became flat. The photocatalytic behavior of raw diatom frustules as catalyst under same conditions showed no degradation of the dye.

The rate constants of the photocatalytic reactions for MB dye were also calculated. From the plot in figure 3.16 and 3.17, the RC values in different photocatalytic reactions using DT500 and DT800 catalysts are obtained and listed in table 3.9.

Table 3.9 Determination of RC for photocatalytic reaction using dye MB

Catalyst name	Conc. (μM)	Correlation function R^2		Polynomial equation	RC (min^{-1})
		Linear fitting	Polynomial fitting		
DT500	20	0.92	0.99	$y= -0.00206x^2 + 0.18287x - 0.06769$	0.10
DT800		0.98	0.98	$y= -785421* 10^{-4}x^2 + 0.15228x + 0.05028$	0.13
DT500	50	0.90	0.99	$y = 5.86256* 10^{-4}x^2 - 0.0033x + 0.04208$	0.05
DT800		0.95	0.99	$y = 0.00107x^2 + 0.02994x + 0.05336$	0.094

It was observed that (table 3.9) the RC values for the reaction using DT800 catalyst were more in case of both 20μM and 50μM dye concentration than that using DT500 catalyst. This confirmed that DT800 catalyst speed up the reaction faster than DT500 catalyst.

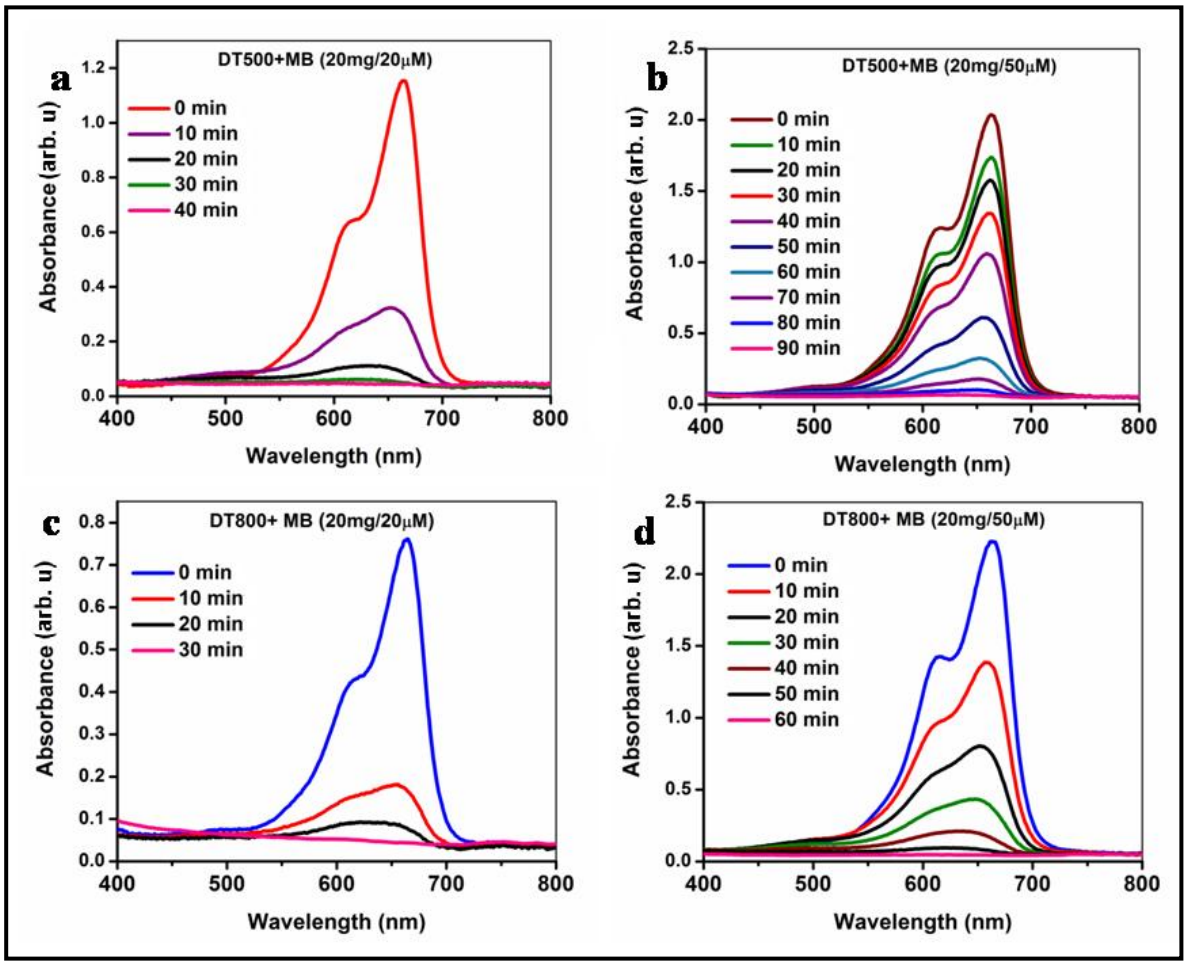

Figure 3.15 Absorption spectra of MB under visible light irradiation for different photodegradation times with a dye concentration of (a) 20μM and (b) 50μM in presence of DT500; (c) 20μM and (d) 50μM in presence of DT800 are shown.

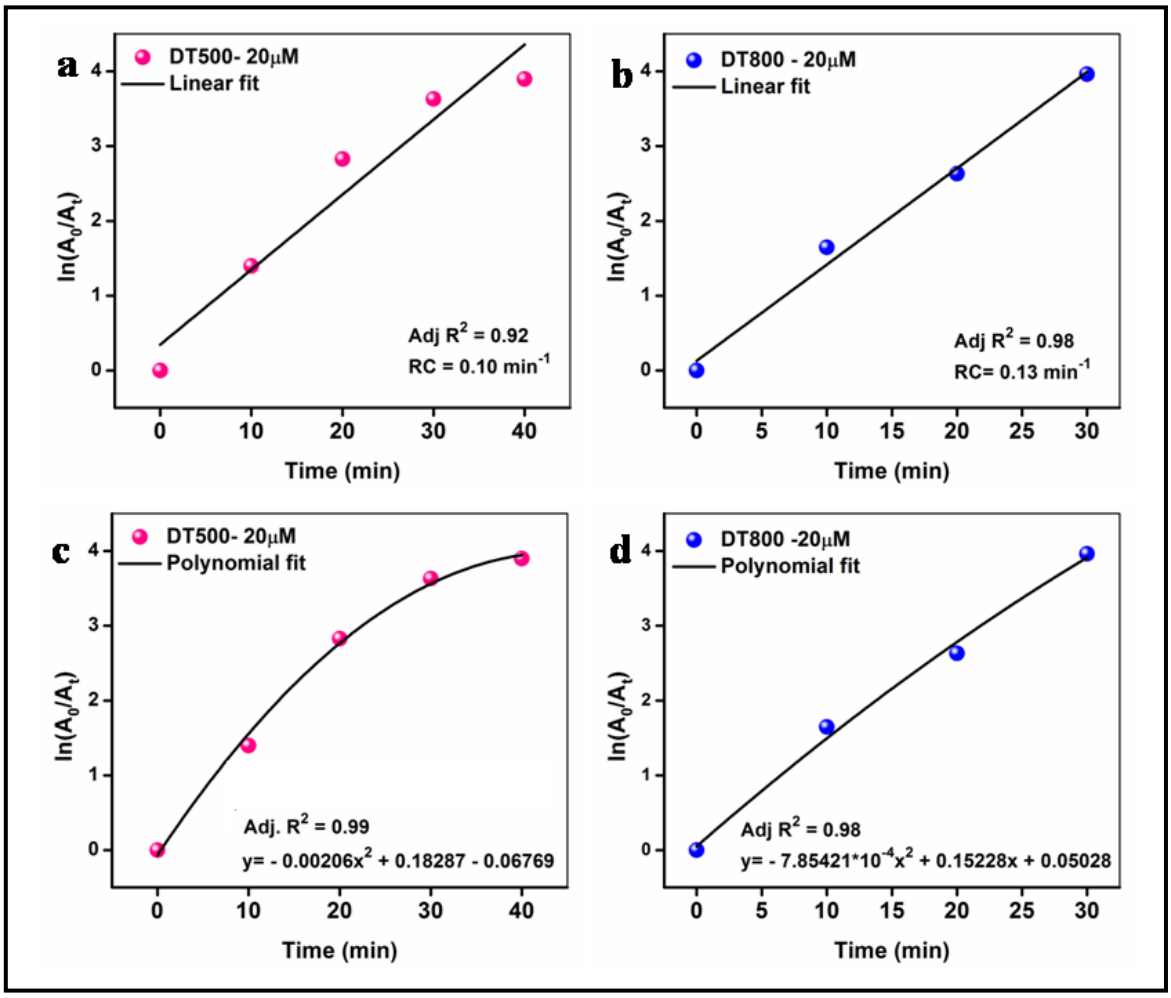

Figure 3.16 Plot of (a & b) linear fitting and (c & d) polynomial fitting to determine RC value for 20μM dye (MB) concentration using catalysts DT500 and DT800 respectively.

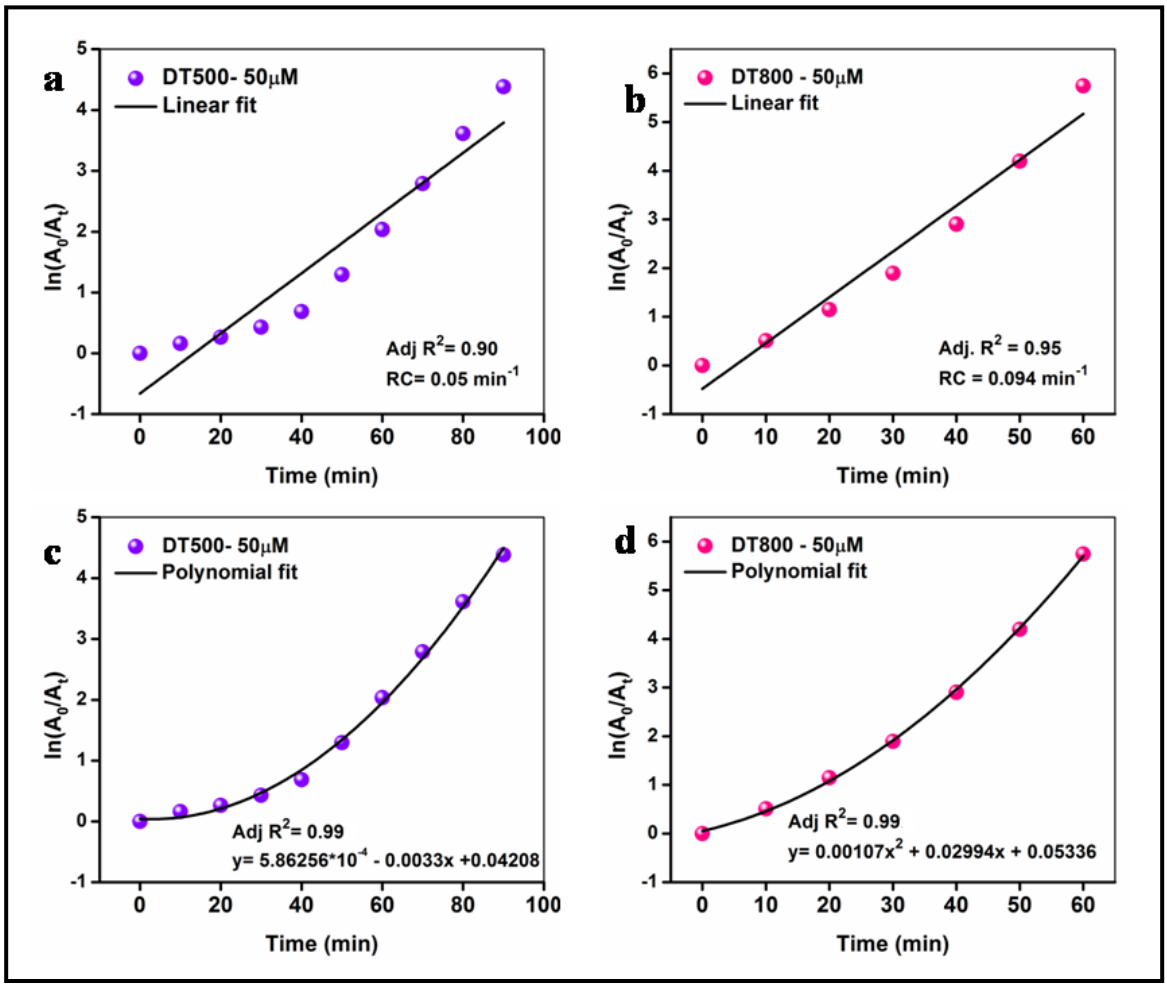

Figure 3.17 Plot of (a & b) linear fitting and (c & d) polynomial fitting to determine RC value for 50μM dye (MB) concentration using catalysts DT500 and DT800 respectively.

3.5 Conclusions

The work in this Chapter leads to the conclusion that an efficient photodegradation process was obtained. The details involving the synthesis of DT800 and DT500, characterization and analyses of their physical properties using various investigative instruments and techniques, finally performing photodegradation observations using dyes have been reported in this chapter. The innovative use of diatoms and TiO_2 nanostructures for these processes is explained. DT800 is shown to be the best candidate for photodegradation compared to DT500, DTiO_2 and diatom frustules. Thus, it has been shown that diatom frustules acting as templates are capable of utilizing a broad range of solar radiation from visible to UV light for very efficient photodegradation processes in combination with proper photocatalysts.

[Note: This work is published in "Journal of Photochemistry and Photobiology A:Chemistry".

Chetia, L., Kalita, D. and Ahmed, G. A. Enhanced photocatalytic degradation by diatom templated mixed phase titania nanostructure. *Journal of Photochemistry and Photobiology A:Chemistry*, 338:134-145, 2017. DOI:10.1016/j.jphotochem.2017.01.035.]

References

[1] Channei, D., Inceesungvorn, B., Wetchakun, N., Ukritnukun, S., Nattestad, A., Chen, J. and Phanichphant, S. Photocatalytic Degradation of Methyl Orange by CeO_2 and Fe–doped CeO_2 Films under Visible Light Irradiation. *Scientific Reports*, 4: 5757, 2014. DOI: 10.1038/srep05757

[2] He, J., Chen, D., Li, Y., Shao, J., Xie, J., Sun, Y., Yan, Z. and Wang, J. Diatom-templated $TiO_2$with enhanced photocatalytic activity:biomimetics of photonic crystals. *Applied Physics A Materials Science and Processing*, 113: 327-332, 2013. DOI: 10.1007/s00339-013-7970-2

[3] Tommasi, E. De., Rea, I., Stefano, L. De., Dardano, P., Caprio, G. Di., Ferrara, M. A. and Coppola, G. Optics with diatoms: towards efficient, bioinspired photonic devices at the micro-scale. In *Proc. SPIE 8792, Optical Methods for Inspection, Characterization, and Imaging of Biomaterials*, volume 8792, Munich, Germany, 2013. DOI:10.1117/12.2021613

[4] Fuhrmann, T., Landwehr, S., Rharbi-Kucki, M. E. and Sumper, M. Diatoms as living photonic crystals. *Applied Physics B Lasers and Optics*, 78:257-260, 2004. DOI: 10.1007/s00340-004-1419-4

[5] Gogoi, A., Buragohain, A. K., Choudhury, A. and Ahmed, G. A. Laboratory measurements of light scattering by tropical fresh water diatoms. *Journal of Quantitative Spectroscopy and Radiative Transfer*, 110: 1566–1578, 2009. DOI:10.1016/j.jqsrt.2009.03.008

[6] Su, Y., Yang, Y., Zhang, H., Xie, Y., Wu, Z., Jiang, Y., Fukata, N., Bando, Y. and Wang, Z. L. Enhanced photodegradation of methyl orange with TiO_2 nanoparticles using a triboelectric nanogenerator. *Nanotechnology*, 24: 295401, 2013. DOI:10.1088/0957-4484/24/29/295401

[7] Carmen, Z. and Daniela, S. Textile Organic Dyes –Characteristics, Polluting Effects and Separation/Elimination Procedures from Industrial Effluents-A Critical Overview, In Dr. Puzyn, T., editor. *Organic Pollutants Ten Years After the Stockholm Convention Environmental and Analytical Update*. ISBN: 978-953-307-917-2, In Tech, 2012.

[8] Kaur, J., Bansal, S. and Singhal, S., Photocatalytic degradation of methyl orange using ZnO nanopowders synthesized via thermal decomposition of oxalate precursor method. *Physica B*, 416:33-38, 2013. DOI:10.1016/j.physb.2013.02.005

[9] Chen, T., Zheng, Y., Lin, J. M. and Chena, G. Study on the Photocatalytic Degradation of Methyl Orange in Water Using Ag/ZnO as Catalyst by Liquid Chromatography Electrospray Ionization Ion-Trap Mass Spectrometry. *Journal of the American Society for Mass Spectrometry*, 19:9971003, 2008. DOI:10.1016/j.jasms.2008.03.008

[10] Spurr, R. A. and Myers, H. Quantitative Analysis of Anatase-Rutile Mixtures with an X-Ray Diffractometer. *Analytical Chemistry*, 29:760-762, 1957. DOI: 10.1021/ac60125a006

[11] Taylor, J. C., Harding, W. R. and Archibald, C. G. M. An Illustrated Guide to Some Common Diatom Species from South Africa, Report to the Water Research Commission. Technical Report No. TT 282/07, Water Research Commission, Private Bag X03, Gezina 0031, Pretoria, South Africa, 2007.

[12] Sing, K. S. W., Everett, D. H., Haul, R. A. W., Moscou, L., Pierotti, R. A., Rouquerol, J. and Siemieniewska, T. 2008. Reporting Physisorption Data for Gas/Solid Systems. In *Handbook of Heterogeneous Catalysis*, pages 1217-1230, ISBN: 9783527610044, 2008. DOI: 10.1002/9783527610044

[13] Yan, J., Wu, G., Guan, N., Li, L., Li, Z. and Cao, X. Understanding the effect of surface/bulk defects on the photocatalytic activity of TiO2: anatase versus rutile. *Physical Chemistry Chemical Physics*, 15: 10978-10988, 2013. DOI: 10.1039/c3cp50927c

[14] Zhang, W. F., He, Y. L., Zhang, M. S., Yin, Z. and Chen, Q. Raman scattering study on anatase TiO2 nanocrystals. *Journal of Physics D: Applied Physics*, 33:912-916, 2000. DOI: 10.1088/0022-3727/33/8/305

[15] Frank, O., Zukalova, M., Laskova, B., Kurti, J., Koltai, J. and Kavan, L. Raman spectra of titanium dioxide (anatase, rutile) with identified oxygen isotopes (16, 17, 18). *Phys. Chem. Chem. Phys*., , 14:14567-14572, 2012. DOI: 10.1039/c2cp42763j.

[16] *Raman data and analysis, Raman Spectroscopy for Analysis and Monitoring*. Retrieved on 06 August 2016 from http://www.horiba.com/fileadmin/uploads/Scientific/Documents/Raman/bands.pdf

[17] Mali, S. S., Betty, C. A., Bhosalec, P. N. and Patil, P. S. Hydrothermal synthesis of rutile TiO2 with hierarchical microspheres and their characterization. *Cryst. Eng. Comm.*, 13: 6349- 6351, 2011. DOI: 10.1039/c1ce05928a

[18] Paul, S. and Choudhury, A., Investigation of the optical property and photocatalytic activity of mixed phase nanocrystalline titania. *Applied Nanosciencs*, 4:839-847, 2014. DOI: 10.1007/s13204-013-0264-3

[19] Man, Y., Mu, L., Wang, Y., Lin, S., Rempel, G. L. and Pan, Q. Synthesis and Characterization of Rutile Titanium Dioxide/Polyacrylate Nanocomposites for Applications in Ultraviolet Light-Shielding Materials. *Polymer Composites*, 36: 2014. DOI:10.1002/pc.22903

[20] Vasconcelos, D. C. L., Costa, V. C., Nunes, E. H. M., Sabioni, A. C. S., Gasparon, M. and Vasconcelos, W. L. Infrared Spectroscopy of Titania Sol-Gel Coatings on 316L Stainless Steel. *Materials Sciences and Applications*, 2: 1375-1382, 2011. DOI:10.4236/msa.2011.210186

[21] Bagheri, S., Shameli, K. and Hamid, S. B. A. Synthesis and Characterization of Anatase Titanium Dioxide Nanoparticles Using Egg White Solution via Sol-Gel Method. *Journal of Chemistry*, 2013: 848205, 2013. DOI: 10.1155/2013/848205

[22] Stuart, B. *Infrared Spectroscopy: Fundamentals and Applications*, John Wiley & Sons, 2004. ISBN: 978-0-470-85428-0.

[23] Devi, R. S., Venckatesh, R. and Sivaraj, R., Synthesis of Titanium Dioxide Nanoparticles by Sol-Gel Technique. *International Journal of Innovative Research in Science, Engineering and Technology*, 3: 15206-15211, 2014. DOI: 10.15680/IJIRSET.2014.0308020

[24] Danwittayakul, S., Jaisai, M., Koottatep, T. and Dutta, J. Enhancement of Photocatalytic Degradation of Methyl Orange by Supported Zinc Oxide Nanorods/Zinc Stannate (ZnO/ZTO) on Porous Substrates. *Industrial & Engineering Chemistry Research*, 52:13629-13636, 2013. DOI: 10.1021/ie4019726.

[25] Borah, M. and Mohanta, D. Structural and optoelectronic properties of E^{u2+}- doped nanoscale barium titanates of pseudo-cubic form. *J. Appl. Phys*., 112: 124321- 8, 2012.

[26] Choudhury, B. and Choudhury, A., Oxygen defect dependent variation of bandgap, Urbach energy and luminescence property of anatase, anatase–rutile mixed phase and of

rutile phases of TiO2 nanoparticles. *Physica E*, 56:364-371, 2014. DOI: 10.1016/j.physe.2013.10.014

[27] Paul, S., Chetri, P., Choudhury, B., Ahmed, G. A. and Choudhury, A. Enhanced visible light photocatalytic activity of Gadolinium doped nanocrystalline titania: An experimental and theoretical study. *Journal of Colloid and Interface Science*, 439:54-61, 2015. DOI: 10.1016/j.jcis.2014.09.083

[28] Mao, L., Liu, J., Zhu, S., Zhang, D., Chen, Z. and Chen, C. Sonochemical fabrication of mesoporous TiO2 inside diatom frustules for photocatalyst. *Ultrasonics Sonochemistry*, 21:527-534, 2014. DOI: 10.1016/j.ultsonch.2013.09.001

[29] Stefano, L. D., Rea, I., Rendina, I., Stefano, M. D. and Moretti, L. Lensless light focusing with the centric marine diatom Coscinodiscus walesii. *Optical Express*,24: 18082-18088, 2007. DOI: 10.1364/OE.15.018082

[30] Cabrera, R. Q., Vazquez, C. S., Bear, J. C., Darr, J. A. and Parkin, I. P. Photocatalytic Evidence of the Rutile-to-Anatase Electron Transfer in Titania.*Advanced Materials Interfaces*, 1: 1400069, 2014. DOI: 10.1002/admi.201400069

[31] Baxter, R. J. and Hua, P. Insight into why the Langmuir–Hinshelwood mechanism is generally preferred. *Journal of Chemical Physics*, 116(11):4379-4381, 2002. DOI:10.1063/1.1458938

[32] Kar, R., Gupta, O., Mandol, K. and Bhattacharjee, S. Performance Study on Photocatalysis of Phenol Solution in a UV Irradiated Reactor.*Journal of Chemical Engineering & Process Technology*, 4: 1000143, 2013. DOI: 10.4172/2157-7048.1000143).

[33] Sahoo,C., Gupta, A. K. and Pillai, I. M. S. Heterogeneous photocatalysis of real textile wastewater: Evaluation of reaction kinetics and characterization, *Journal of Environmental Science and Health, Part A*, 47:2109-2119, 2012. DOI: 10.1080/10934529.2012.695996).

[34] Yizhong, W. Photocatalytic decolorization characteristics of various dyes with different structures, *Toxicological & Environmental Chemistry*, 70: 67-79, 2008. DOI: 10.1080/ 02772249909358740.